Reversed Lateral Circulation in a Sharp Estuarine Bend with Weak Stratification

WOUTER M. KRANENBURG[a] AND W. ROCKWELL GEYER

Woods Hole Oceanographic Institution, Woods Hole, Massachusetts

ADRIAN MIKHAIL P. GARCIA

Woods Hole Oceanographic Institution, Woods Hole, and Massachusetts Institute of Technology, Cambridge, Massachusetts

DAVID K. RALSTON

Woods Hole Oceanographic Institution, Woods Hole, Massachusetts

(Manuscript received 27 August 2018, in final form 17 April 2019)

ABSTRACT

Although the hydrodynamics of river meanders are well studied, the influence of curvature on flow in estuaries, with alternating tidal flow and varying water levels and salinity gradients, is less well understood. This paper describes a field study on curvature effects in a narrow salt-marsh creek with sharp bends. The key observations, obtained during times of negligible stratification, are 1) distinct differences between secondary flow during ebb and flood, with helical circulation as in rivers during ebb and a reversed circulation during flood, and 2) maximum (ebb and flood) streamwise velocities near the inside of the bend, unlike typical river bend flow. The streamwise velocity structure is explained by the lack of a distinct point bar and the relatively deep cross section in the estuary, which means that curvature-induced inward momentum redistribution is not overcome by outward redistribution by frictional and topographic effects. Through differential advection of the along-estuary salinity gradient, the laterally sheared streamwise velocity generates lateral salinity differences, with the saltiest water near the inside during flood. The resulting lateral baroclinic pressure gradient force enhances the standard helical circulation during ebb but counteracts it during flood. This first leads to a reversed secondary circulation during flood in the outer part of the cross section, which triggers a positive feedback mechanism by bringing slower-moving water from the outside inward along the surface. This leads to a reversal of the vertical shear in the streamwise flow, and therefore in the centrifugal force, which further enhances the reversed secondary circulation.

1. Introduction

Like rivers, natural tidal channels often exhibit meandering planforms (Fagherazzi et al. 2004; Dalrymple and Choi 2007). The channel curvature influences the flow structure, which affects transport of dissolved and suspended matter and feeds back into the morphological development. Although the hydrodynamics of river meanders are well studied (e.g., already by Boussinesq 1868; Thomson 1877; see also Apmann 1964), the influence of curvature on the flow in estuaries is less well understood.

In rivers bends, curvature causes a secondary flow in the plane perpendicular to the depth-averaged flow direction: the curvature induces a centrifugal acceleration (CFA), which is strongest in the upper part of the water column where the streamwise velocity is maximal. The centrifugal motion generates a water level setup on the outside of the bend and a setdown on the inside (superelevation). This causes an inward-directed barotropic pressure gradient force that is uniform over the depth. The local imbalance between the centrifugal

Denotes content that is immediately available upon publication as open access.

[a] Current affiliation: Deltares, Delft, Netherlands.

Corresponding author: Wouter M. Kranenburg, wouter.kranenburg@deltares.nl

DOI: 10.1175/JPO-D-18-0175.1

acceleration and barotropic pressure force in the vertical generates a secondary flow directed toward the inside of the bend near the bed and toward the outside at the surface, resulting in a helical flow pattern along the bend (Boussinesq 1868; Thomson 1877). Analytical solutions for the secondary flow profile have been provided by Rozovskii (1957), and, for example, Engelund (1974) and Kalkwijk and Booij (1986). The circulation causes sediment transport toward the inner bank, and as a result in alluvial meanders shallow areas called point bars are formed at the inside of bends and deeper scour zones called pools are formed at the outside (Leopold and Wolman 1960).

The curvature also influences the streamwise flow: the adaptation of the transverse surface slope with changing curvature leads to a transverse gradient in the along-river pressure gradients. As a result, the inner bend flow accelerates and the outer bend flow decelerates while entering the bend, resulting in an inward-skewed velocity distribution, like a free vortex/potential flow (Johannesson and Parker 1989; Seminara 2006), and the sharper the bend, the stronger this effect. However, the increase of bottom friction with velocity limits this development. Reduced depth and a point bar in the inside of the bend further enhance friction (Blanckaert and de Vriend 2010), and topographically redistribute streamwise momentum toward the outside (Dietrich and Smith 1983; Blanckaert 2010). This promotes an excess of streamwise velocity in the deeper part of the cross section near the *outer* bank, as is often found in natural rivers. The secondary circulation can also influence the streamwise flow structure. Their interaction can create an additional, smaller, counterrotating circulation cell near the surface at the outside of the bend (de Vriend and Geldof 1983; Blanckaert and de Vriend 2004), and for strongly curved bends advection of streamwise momentum by lateral circulation can lead to nonmonotonic velocity profiles (Blanckaert and Graf 2004). The latter yields a negative feedback on the secondary circulation (Blanckaert 2009), and consequently on the transverse bed slope development, topographic steering, and ultimately the meander migration (Blanckaert 2011). The relative importance of the mechanisms for lateral redistribution of streamwise momentum along the bend depends on the parameters $c_f^{-1}H/R$ and W/R (Blanckaert and de Vriend 2010) where c_f is the friction coefficient, H the water depth, W the channel width, and R the channel radius of curvature. These parameters are both small in mildly curved bends but $O(1)$ in sharp bends.

In estuaries, the alternating tidal flow, varying water level and presence of salinity gradients further complicate the dynamics. Horizontal salinity gradients can drive lateral circulation even in straight estuarine channels. In a well-mixed estuary Nunes and Simpson (1985) found during flood tide two counterrotating circulation cells with flow toward the sides near the bed and convergent flow at the surface, explained by saltier water moving faster in the middle of the channel (differential advection) to create lateral salinity gradients driving the lateral circulation. In curved flow, weak vertical salinity gradients (stratification) can strengthen the secondary circulation (Geyer 1993; Dronkers 1996) by strengthening of the vertical shear in the streamwise flow and reducing the frictional damping by reducing turbulence. In fast-moving, weakly stratified flows, the lateral circulation can overturn and mix the water column, resulting in the cross-channel velocities becoming consistent again with those for unstratified flow (Seim and Gregg 1997). However, sufficiently strong stratification will suppress the circulation, as the secondary circulation generates a setup of saltwater in the inner bend, thus inducing a baroclinic pressure gradient force (BCPF) counteracting the ''classical'' secondary circulation (Chant and Wilson 1997). In partially stratified estuaries, which are sometimes mixed but also sometimes stratified for a full tidal cycle depending on the competition between buoyancy and mixing, the strength of this mechanism varies strongly with river discharge and tidal forcing (Chant 2002). Time lags between the spinup and disappearance of the centrifugal acceleration and the response of the baroclinic gradient can result in an internal lateral seiche and along-channel adjustment of the lateral circulation, due to an unsteady balance between CFA and BCPF (Lacy and Monismith 2001). This can cause the vertical structure to change from classical secondary circulation to a three-layer structure with outward flow near the bed, to even a reversed circulation cell (Nidzieko et al. 2009).

The dynamics of bend flow in estuaries are not necessarily symmetric for ebb and flood. Differences can be induced by, for example, differences in strength (Friedrichs and Aubrey 1988) or vertical profile of ebb and flood currents. The latter can result from asymmetry in the along estuary baroclinic gradient force with respect to the tidal flow, which generally enhances shear (Chant and Wilson 1997) and stratification (Simpson et al. 1990) during ebb, but can lead to a near-bed maximum in the streamwise flow during flood, which affects the centrifugal acceleration and secondary flow (Winterwerp et al. 2006). Streamwise flow with a near-bed maximum and reversed secondary circulation during flood has also been observed in the absence of an along-estuary salinity gradient (Nakayama et al. 2016), attributed to asymmetry in tidal advection. Ebb–flood differences in secondary flow may also be induced by

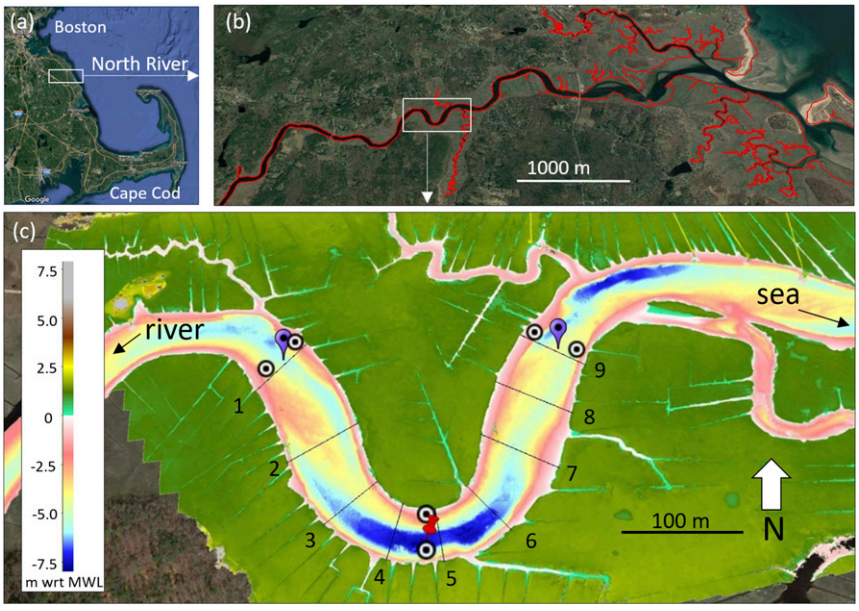

FIG. 1. The North River. (a) Location; (b) outline, with location of the studied bend (white rectangle); (c) bend bathymetry and field work setup. Black lines 1–9: ADCP survey tracks; CTD casts in cross sections 1, 3, 5, 7, and 9; red pin: apex mooring with CTDs and a bottom frame mounted Aquadopp profile current meter. Purple balloons: moorings with surface and bottom CTs. Circles: CTDs (near bottom).

differences in lateral salinity gradients (Lacy and Monismith 2001; Winterwerp et al. 2006), resulting from lateral differences in streamwise velocity produced by, for example, confluences, harbors, or local geometric features. In a numerical study of an idealized, partially stratified estuary, Pein et al. (2018) found persistent secondary circulation during ebb and reversed circulation at the end of flood, explained by an ebb–flood asymmetry in differential advection leading to a lateral baroclinic pressure gradient force acting with the centrifugal force during ebb and against it during flood. Ebb–flood asymmetry could also be induced by varying water levels, affecting the friction, and by asymmetry in the sense of the Coriolis force w.r.t. the centrifugal force, though the latter is generally negligible on the scale of estuarine bends (Geyer 1993; Buijsman and Ridderinkhof 2008).

Most studies in estuaries consider relatively mild bends [e.g., maximum W/R of about 0.3 in Nidzieko et al. (2009)] and are in partially stratified estuaries. If stratification is weak or absent then the baroclinic inhibition of secondary flow by tilting of the pycnocline will be unimportant. In this study we investigate the influence of a high curvature bend on the flow and salinity structure in an intermittently stratified estuary. We focus especially on asymmetry in the secondary flow between maximum flood and ebb, when stratification is negligible. Using observations of pressure, streamwise velocity and salinity, we identify and quantitatively verify the mechanism leading to this asymmetry. We discuss how spring-neap differences affect the secondary flow, how our observations relate to bend effects described in literature, and what conditions are necessary for the phenomena we observe to occur in general.

2. Methods

a. Field site

We carried out a field study in the North River estuary (Massachusetts, United States), a narrow, meandering salt-marsh creek, that flows into Massachusetts Bay and the Atlantic Ocean (see Fig. 1). The tidal range at the mouth of the North River varies between 2 and 3.5 m. The North River discharge, estimated from catchment area and USGS discharge measurements in a contributory stream upriver (station 01105730), is rain-event dominated with peaks up to about 40 $m^3 s^{-1}$ but generally much smaller, especially in the summer (Fig. 2). Typical midestuary dimensions are a channel width of about 50 m and a mean depth of about 5 m (aspect ratio $W/H \approx 10$). Bends have width-to-radius-of-curvature ratios of up to $W/R \approx 1$, which is as high as strongly meandering rivers. The channel features steep banks adjoining broad intertidal marshes, which typically are inundated only during spring high tides.

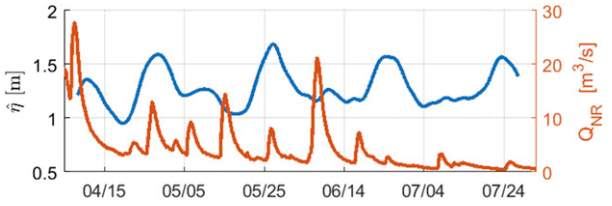

FIG. 2. Characteristic forcing for the North River: blue is water level amplitude at the seaward side of the North River, and red is estimated river discharge

The focus of this study is a sharp bend about 5.5 km from the mouth of the estuary (see Figs. 1b,c). In the apex of the bend, $W \approx 50$ m, $H \approx 6$ m [w.r.t. mean water level (MWL)] and $R \approx 70$ m, and the distance along the bend from the upriver to the downriver inflection point is about 350 m. Although the inside of the bend has a more gently sloping bed than the outside, the cross sections around the apex do not show a distinct point bar as is usually found in alluvial rivers (see Fig. 3c).

b. *Instrumentation*

As part of a larger instrument deployment, time series measurements of current profiles and water properties were obtained in the apex of the bend, about 15 m from the outside, over the period from 4 April to 31 July 2017 (location: red pin in Fig. 1c). An upward-looking Aquadopp Profiler (cell size 0.20 m, profile interval 10 min, averaging period 45 s) was mounted on a bottom frame along with five temperature–salinity–pressure sensors on a line through the water column (sample period 2 min). From 24 to 31 July 2017, four temperature–salinity and six temperature–salinity–pressure sensors (sample period 1 min) were deployed up- and downestuary of the bend in the channel center and near the banks. Shipboard measurements were collected on 24, 25, 28, and 31 July, including acoustic Doppler current profiler (ADCP) measurements (cell size 0.50 m, profile interval 0.25 s) over nine transects, and temperature–salinity profile measurements (continuous casts, sample frequency 12 Hz) over transects 1, 3, 5, 7, and 9 (see Fig. 1c). The transects were repeated about every 30 min from transect 1 to 9, with the temperature–salinity measurements generally carried out while transiting from north to south, that is, from the inside to the outside of the bend, in less than a minute.

c. *Data processing*

The moored velocity data were processed to yield vertical profiles of streamwise and stream-normal (secondary) velocity by rotating the data toward the direction of the depth-averaged flow. Prior to this, the data in the most upper part of the water column, where

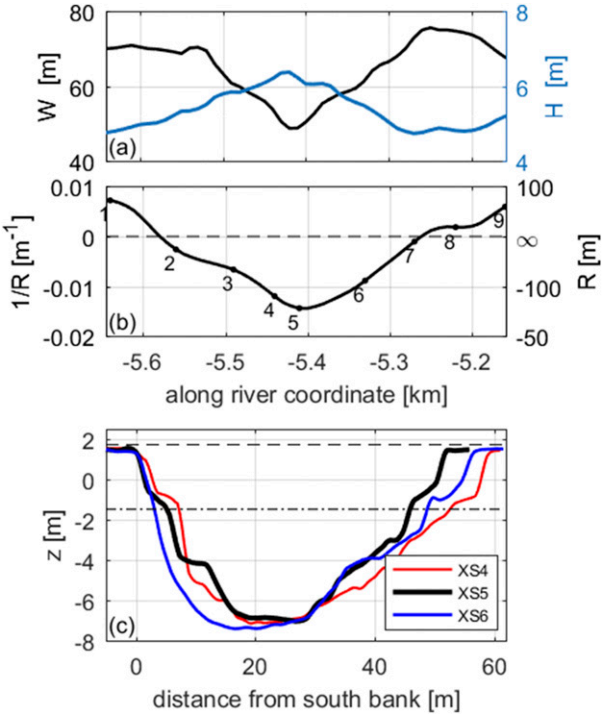

FIG. 3. Bend geometry. (a) Width W and depth H (cross section averaged); (b) curvature $1/R$; (c) three cross-sectional depth profiles in the bend, with $z = 0$ the level of MWL, the dashed line is the mean higher high water (MHHW), and the dash–dotted line is the mean lower low water (MLLW). The south bank is the outside of the bend.

reflection by the water surface influences the measurements, were removed. The shipboard ADCP data were processed by interpolating the measured northward and eastward flow velocities onto regular grids at each cross section ($\Delta y = 1$ m, $\Delta z = 0.5$ m), smoothing the data with a boxcar filter ($l_y = 5$ m, $l_z = 0.5$ m, with l the filter length), and rotating the data toward the direction of the depth-averaged flow at each grid cell in the lateral. With this approach the angle of rotation varies slightly across the cross section, but it clearly separates the depth-varying component of secondary flow from the primary flow, as the depth-averaged stream-normal velocity is zero for each y coordinate. An estimate of the vertical velocities over the cross section was obtained by vertically integrating the stream-normal gradients of the stream-normal velocity (thus neglecting the contributions from streamwise gradients).

The near-bank pressure measurements were processed to yield relative water level elevations by shifting the signal for each sensor such that it is zero at the flow reversal preceding the ebb/flood of interest (this assumes a horizontal water surface at slack tide). A time series was determined for the mean of the shifted signals and subtracted from the shifted signals, resulting in

relative water levels for each sensor. The sensor at the north side of cross section 1 did not work properly, so because curvature is limited there we assumed a time series equal to the sensor on the south side. The horizontal salinity gradient $\partial s/\partial x$ along the bend was computed between the average salinity at cross section 9 and cross section 1. Representative stratification was calculated from the average of the top–bottom salinity difference for the three moorings.

3. Observations

a. Estuarine conditions

The tidal amplitude during the deployment varied between 1.7 m at the spring tide on 24 July and 1.0 m at the neap tide on 31 July, with a daily inequality particularly around the spring tide (Fig. 4a). Both the spring-neap variation and daily inequality of the tide are also visible in the depth-averaged velocity $\langle u \rangle$ in the bend (Fig. 4b), the latter especially in the ebb flow around spring tide. The sudden acceleration and high flood velocity near midnight on 25 July represents the inundation of the marsh platform and abrupt increase in tidal prism. During strong spring tide floods, high salinity (~30 psu) water from Massachusetts Bay flows past the bend (Fig. 4c). The salinity drops significantly during the ebb, about 8 psu during spring tide ebbs and 14 psu during neap tide ebbs. The horizontal salinity gradient $\partial s/\partial x$ along the bend (Fig. 4d) increases from spring to neap, consistent with the length of the salt intrusion decreasing with decreasing tidal amplitude. Stratification Δs (Fig. 4e) occurs only around flow reversals, and as the tidal velocity increases Δs quickly reduces to almost zero. Therefore, we describe this system during our measurements as ''intermittently stratified.''

b. Vertical profiles of lateral and streamwise velocity in the bend apex

Next we examine the vertical profiles of the streamwise and lateral flow at the bend apex mooring (Fig. 5). The marked instances and profiles 1–4 correspond to the times of maximum flood and ebb during the shipboard measurements. The ebb surveys (1 and 2) took place during a strong spring tide ebb and a weak neap tide ebb, but the flood surveys (3 and 4) did not represent the full range of tidal amplitude, so profiles for two additional instances coinciding with a strong spring tide flood (profile 5) and a weak neap tide flood (profile 6) have been plotted.

The vertical profiles of the lateral flow are distinctly different between ebb and flood (Figs. 5b,d). During

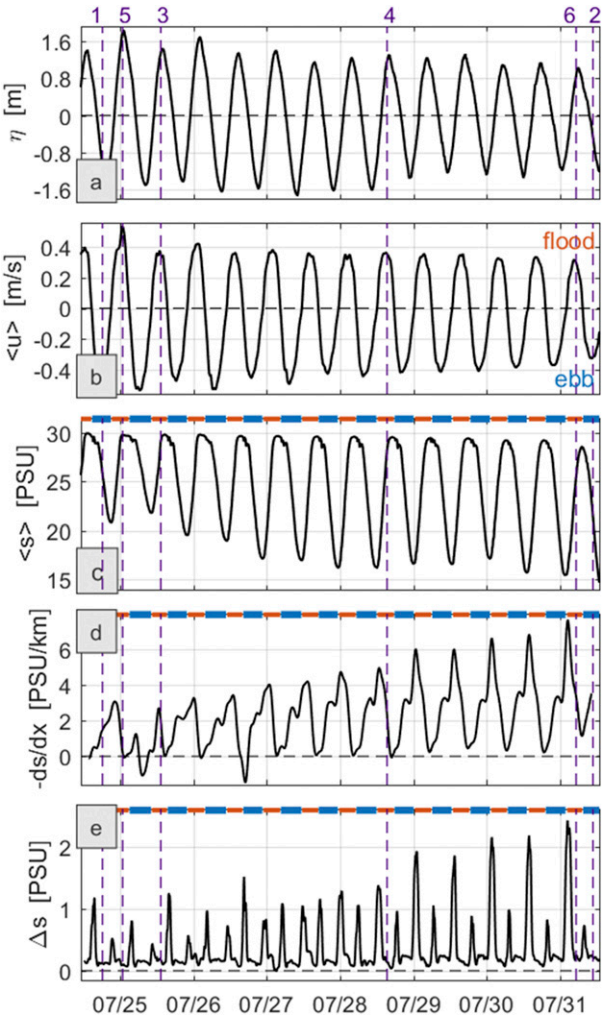

FIG. 4. Conditions in the North River, 24–31 Jul 2017. (a) Water level elevation at the seaward side of the North River. (b) Depth-averaged horizontal flow velocity in the bend (from the Aquadopp in the bend apex). (c) Salinity (average of all sensors in the bend area). (d) Horizontal salinity gradient over the bend area. (e) Stratification. In (c)–(e), the horizontal bar on the top of the graph indicates the tidal phase, with orange indicating the flood phase and blue the ebb phase. The dotted vertical lines indicate the six instances highlighted in Fig. 5.

ebb, a strong secondary circulation is present with the flow directed toward the inside of the bend near the bed and toward the outside near the surface. This circulation, in line with the classical helical circulation for river bends, is observed for all ebb phases in Fig. 5b. During the flood phase no such strong secondary circulation is observed—the near-bed flow is much weaker, with an increasing difference between ebb and flood toward neap tide. Flow toward the outside of the bend is present in the middle of the water column, but near the surface the lateral flow tends toward zero or even positive, inward-directed

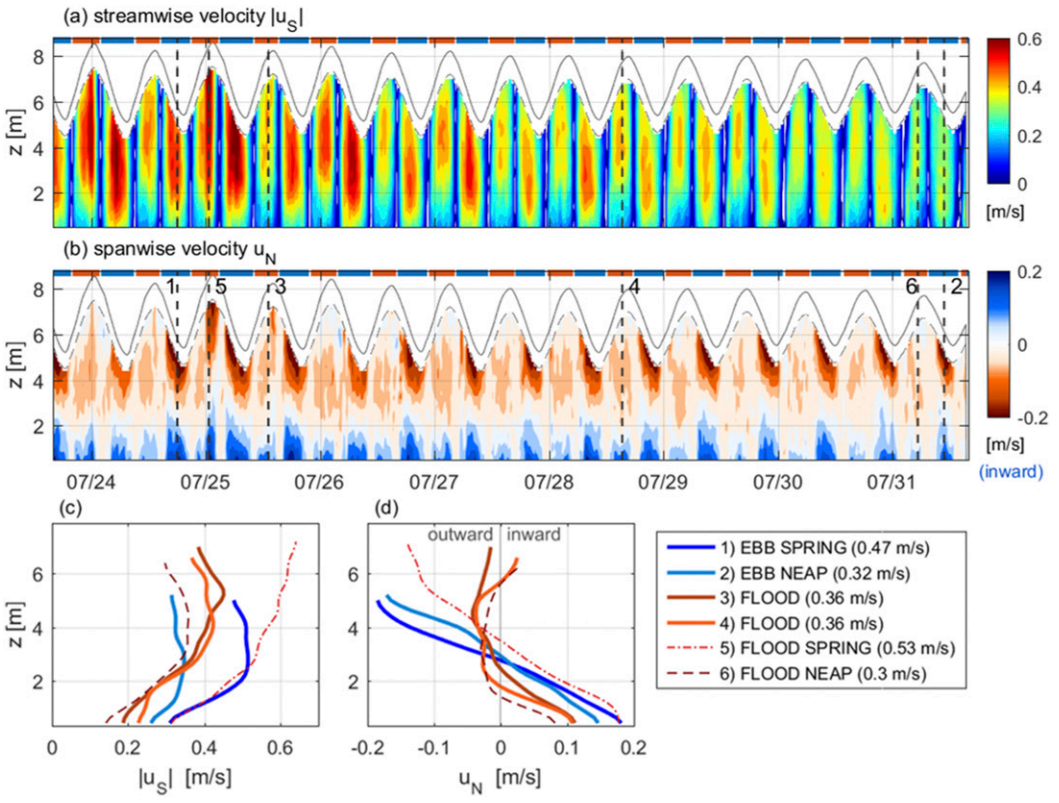

FIG. 5. Flow velocities in the bend apex. (a),(b) The (absolute) streamwise flow velocities respectively lateral (spanwise) flow velocities as function of time and distance above the bed. The dark continuous line indicates the free surface, and the dotted line is the cutoff level. The alternatingly orange (flood) and blue (ebb) horizontal bars on the top of the graph denote the tidal phase. Positive (blueish) velocities in (b) indicate flow directed toward the inside of the bend. (c),(d) Vertical profiles of streamwise respectively lateral flow velocities for instances 1–6 indicated in (a) and (b) with the dotted vertical lines. Source: the profile current meter in the bend apex.

flow. Only once does the flood phase show the classical secondary circulation (instance 5), which is the strongest flood of the record, but only briefly during the second half of the flood.

The streamwise velocities are generally larger during ebbs than during the adjacent flood phases (Fig. 5a). This ebb dominance can be explained from the lower water level and reduced cross-sectional area during maximum ebb compared to maximum flood. The shape of the streamwise velocity profiles is quite similar between ebb and flood—though the flood flow generally shows slightly more shear in the lower part of the profile, in both tidal phases the profile often has a subsurface maximum (the exception being the strong spring tide flood of instance 5).

c. *Cross-sectional structure of lateral velocity in the bend apex*

The cross-sectional structure of the lateral velocity in the bend apex also displays a distinct difference between ebb and flood (Fig. 6). During ebb the secondary flow has a structure as observed in rivers, with flow toward the inner bend near the bed and toward the outer bend near the surface. The circulation, both during spring and neap tide ebb present as a single cell over the cross section, is the strongest during spring tide ebb. During flood, the structure is clearly different, with multiple circulation cells. Over much of the cross section, inward-directed flow is observed near the surface and outward-directed flow at greater depths, though this may not always extend all the way to the bottom. The two flood tides also show strong similarity in structure, but the lateral velocities are stronger during the neap tide survey. The ebb–flood asymmetry in lateral flow is a key observation for this study.

d. *Pressure and streamwise velocity along the bend*

The second most important observation is that during both ebb and flood, the maximum depth-averaged streamwise velocity occurs on the inside of the bend (Fig. 7). Entering the bend, the flow on the

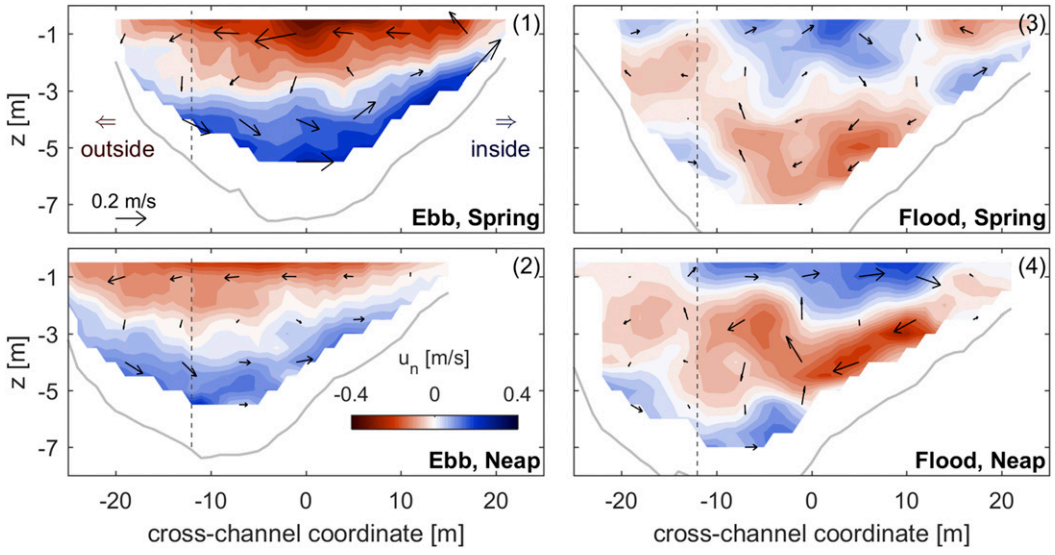

FIG. 6. Lateral flow structure in the cross section in the apex of the bend (Fig. 1c, cross section 5) for maximum (left) ebb and (right) flood, during (top) spring tide and (bottom) neap tide surveys (instances 1–4 in Fig. 5). The inside of the bend is on the right side of the graph. Blue denotes flow toward the inside of the bend and red toward the outside of the bend. Black arrows indicate the magnitude and direction of flow in the cross-sectional plane (with horizontal and vertical velocity scaled the same, unlike the horizontal and vertical distance). For comparison with the profiles in Fig. 5, the dashed line indicates the approximate position of the profile current meter.

inside of the bend accelerates toward the apex and the flow on the outside decelerates. As a result, both for ebb and flood the velocity distribution becomes inwardly skewed, with the maximum not located at the deepest part of the cross section, but rather moving inward approaching the apex. Coming out of the bend, the inner bend flow decelerates and the location of the maximum velocity moves outward, both for ebb and flood.

In the apex of the bend (cross section 5), where the curvature is maximal, we observe lateral water level gradients with setup on the outside of the bend and setdown on the inside (Fig. 7, blue boxes), consistent with the pressure gradient counteracting the centrifugal acceleration of the streamwise flow. From the upstream to the downstream cross section, we observe a decrease in the cross-sectional average water level, which can be explained by frictional and possibly

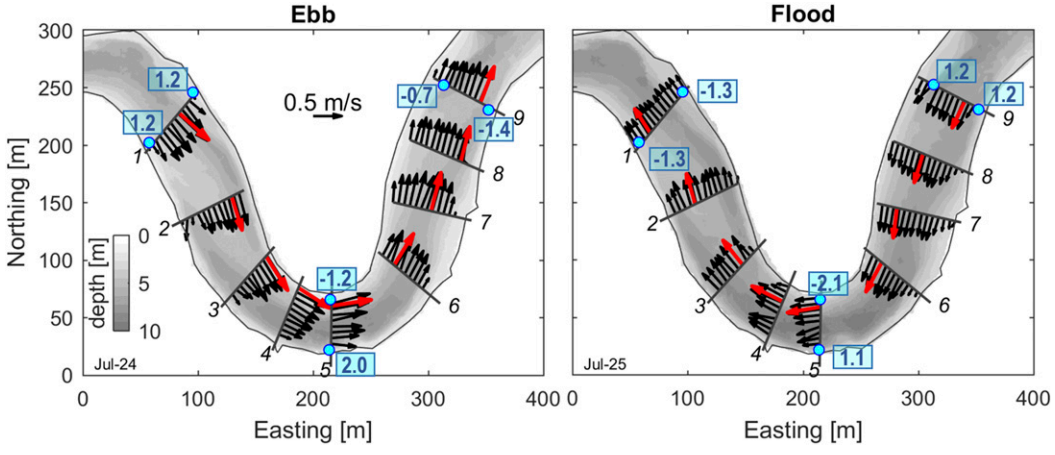

FIG. 7. Depth-averaged velocities and relative water level elevations along the bend at (left) maximum ebb and (right) maximum flood (both for spring tide survey). Red arrows: maximum depth-averaged velocity per cross section. Light blue dots and boxed values: locations of the pressure sensors and belonging relative water level elevations (cm). Black numbers: cross section numbers.

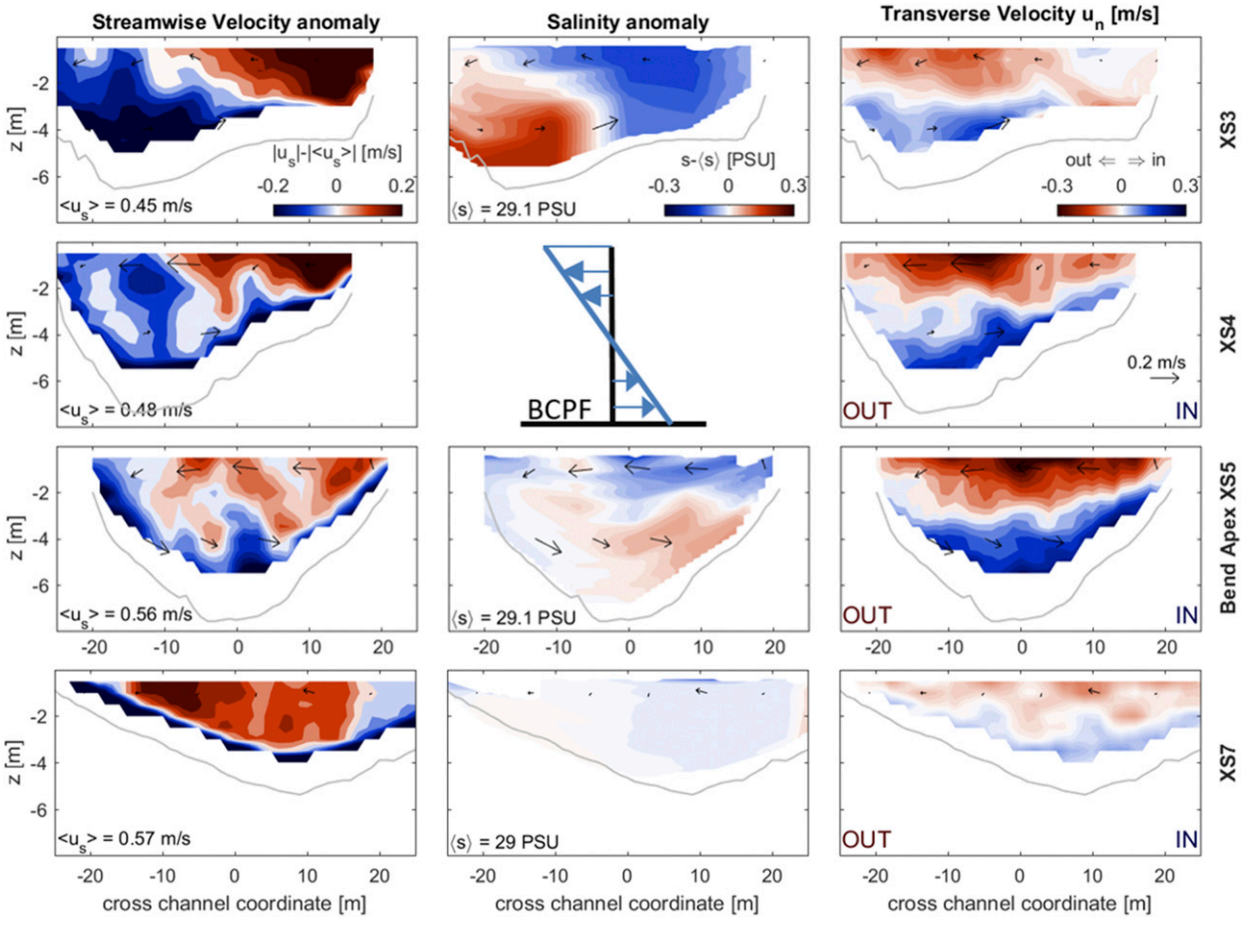

FIG. 8. Ebb case. (left) Streamwise velocity anomaly (i.e., deviation from the cross-sectional mean), (center) salinity anomaly, and (right) stream-normal velocity upstream of the bend in the first and second rows (cross sections 3 and 4, respectively), in the apex of the bend in the third row (cross section 5) and downstream of the bend in the fourth row (cross section 7) for maximum ebb, 24 Jul (spring tide survey, instance 1 in Fig. 5 and Fig. 6). Black arrows indicate flow magnitude and direction in the cross-sectional plane, and ⟨⟩ means cross-section averaged. The inside of the bend is on the right side.

bend-related energy loss. Moving along the estuary, the flow on the inside of the bend experiences a strong pressure drop upstream of the apex, and even adversely directed pressure gradient downstream of the apex. The opposite is the case for the outside of the bend—upstream of the apex the pressure gradient is small or adversely directed, downstream of the bend apex the pressure drop increases. This is consistent with the velocity accelerations and decelerations described above.

The observed maximum streamwise velocity near the inside of the bend and not in the deepest part contrasts typical river flows. It shows the characteristics of a free vortex, and indicates that in this case this potential flow curvature effect is greater than the outward momentum redistribution induced by friction, topographic steering, or secondary flow (Blanckaert 2010). We explain this from the absence of a point bar and the greater relative depth than usually found in alluvial rivers (Williams 1986), already during ebb but even more so during flood tides when the water level is higher.

e. *Cross-sectional structure of velocity and salinity along the bend*

The maximum streamwise velocity occurring near the inside of the bend is also visible in the cross-sectional structure of the streamwise flow, upstream of the apex and in the apex itself during both ebb (Fig. 8) and flood (Fig. 9). However, the cross-sectional salinity structure is distinctly different between ebb and flood (e.g., compare first row middle panels of Figs. 8 and 9): during ebb the salinity is lowest on the inside of the bend (right side), while during flood the salinity on the inside is the highest. These observations are related. The ebb–flood symmetry in lateral distribution of streamwise velocity

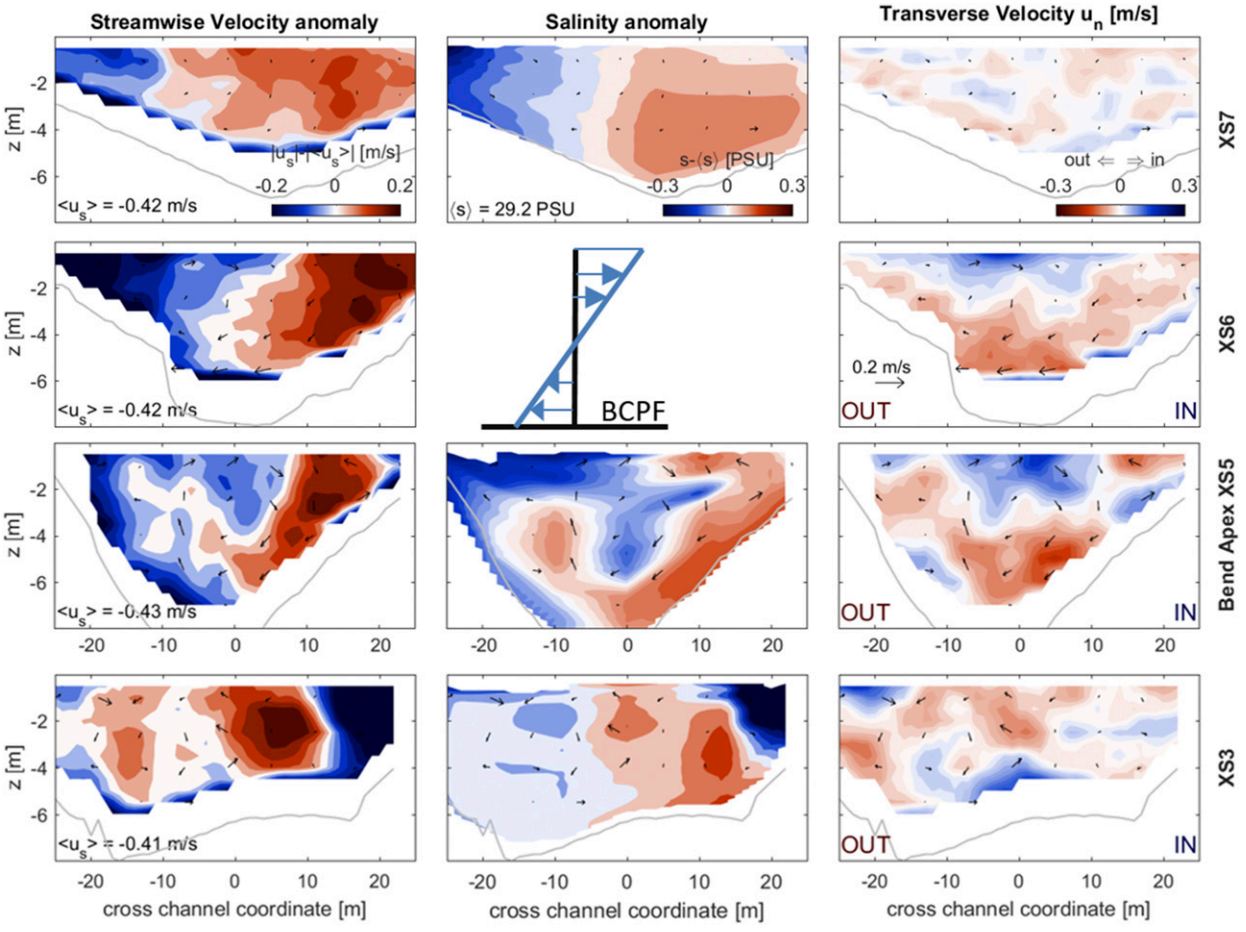

FIG. 9. Flood. (left) Streamwise velocity anomaly, (center) salinity anomaly, and (right) stream-normal velocity upstream of the bend in the first and second rows (cross sections 7 and 6), in the bend apex in the third row (cross section 5), and downstream of the bend in the fourth row (cross section 3) near maximum flood, 25 Jul (spring tide survey, instance 3 in Fig. 5 and Fig. 6). The inner bend is on the right side. Black arrows indicate flow magnitude and direction in the cross-sectional plane. Full disclosure: the results shown actually come from two consecutive survey rounds, with results for cross sections 3, 5, 6, and 7 obtained at 1306, 1311, 1247, and 1250 local time, respectively, so within 20 min from each other.

yields an ebb–flood asymmetry in salinity distribution through advection of the along-estuary salinity gradient: the greater velocity in the inner bend causes the salt-water intrusion during flood to lead at the inside of the bend, while it advects fresher water to the inside of the bend first during ebb.

The lateral velocity (right column) in the bend apex (third row) also is distinctly different between ebb (Fig. 8) and flood (Fig. 9), as mentioned in section 3c. Next, during ebb the structure of the secondary circulation upstream of the bend apex is similar to that in the apex, while during flood the structure of the lateral circulation is more variable through the bend.

The secondary flow is affecting the structure of the streamwise velocity and salinity. During ebb (Fig. 8) the salinity maximum is displaced from the outside of the bend toward the inside, consistent with advection by the secondary flow, while during flood (Fig. 9) the opposite occurs, especially in the middle of the cross section, as saltier water moves outward with the lateral flow lower in the water column. The streamwise velocity is affected similarly: the flow maximum in the inside of the bend is shifted along the surface toward the middle of the channel by the ebb lateral circulation. During flood, the lateral circulation confines the high-momentum region to a small band near the inner bend at the surface, and the high-momentum fluid is advected downward and outward at larger depths.

Beyond the apex (fourth row in Figs. 8 and 9), a low-momentum region forms near the inside of the bend, related to the reversed pressure gradient, and the high momentum region moves outward. The reversed secondary flow present in the apex during flood loses strength and is almost completely gone in cross section 3.

4. Analysis

a. The mechanism (part I)—Baroclinic forcing

Combining the various observations, we explain the ebb–flood asymmetry in the secondary flow as follows: the flow curvature induces a water level setup at the outside of the bend and setdown in the inside, which creates lateral shear in the streamwise velocity with maximum velocities near the inside of the bend. The lateral velocity difference advects fresher water first to the inside of the bend during ebb and saltier water during flood. The lateral salinity difference resulting from this differential advection yields a BCPF (directed from high to low salinity at the bed, shown schematically in the middle panels of Figs. 8 and 9), that enhances the classic helical circulation during ebb and counteracts it during flood. When strong enough, this baroclinic force generates a reversed secondary circulation during flood. This baroclinic force is key to the asymmetry between flood and ebb. However, we will see in sections 4d and 4e that it is not the full explanation.

b. Lateral shear in streamwise momentum

To verify our explanation, we now analyze the various elements of the dynamics quantitatively. The first question is: Can we indeed explain the lateral shear in streamwise velocity from the curvature induced pressure gradients? To answer this, we estimate the change in momentum along two streamlines in the bend around the time of maximum flood, for which we approximate the streamwise momentum balance by considering along-channel advection, pressure gradient and bottom friction (neglecting lateral momentum exchange):

$$u\frac{\partial u}{\partial \chi} = -g\frac{\partial \eta}{\partial \chi} - \frac{c_f u|u|}{H}. \tag{1}$$

Here u denotes depth-averaged streamwise velocity, χ the along-streamline distance (the symbol s will denote the along-stream coordinate measured in the centerline), c_f the quadratic friction coefficient, and H the depth. We calculate the velocity increase from upstream toward the bend apex near the inside of the bend and the velocity decrease near the outside for maximum flood on 25 July, by applying this equation on (depth-averaged) streamlines from cross section 9 to 5. To compute the pressure term we use the relative water levels (Fig. 7) and the distance between the sensors along the inner and outer bend. To compute the friction term, the velocity is assumed to change linearly along the streamline (which introduces a small error relative to the pressure uncertainty), and a friction factor of

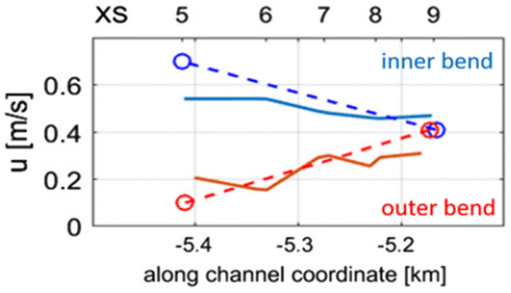

FIG. 10. Streamwise velocity (depth averaged): measured (solid) vs calculated (dashed) in the inside (blue) and outside (red) of the bend. For maximum flood, 25 Jul.

$c_f = 3 \times 10^{-3}$ is adopted (consistent with direct covariance estimates of stress, and a common value in literature). The results (Fig. 10) show that the observed pressure gradient anomaly due to curvature is sufficient to be the driver of the observed cross-channel velocity variation. Actually, the lateral shear is overestimated, which is consistent with neglecting the lateral mixing and advection terms Eq. (1) that would tend to reduce the lateral shear.

Additionally, we explore what velocity distribution can be expected for the bend based on the competition between the inward redistribution of streamwise momentum by the free vortex effect and the outward distributing mechanisms like friction and topographic steering, and how this depends on channel geometry. For this we use the model for momentum redistribution in curved open channels derived from the streamwise momentum equation by Blanckaert and de Vriend (2003, 2010). This model explicitly considers the abovementioned processes and yields a first-order approximation of the lateral distribution of the streamwise velocity and its development along a bend for a given geometry and mean velocity. Details on the model application are reported in appendix A. The main result is that the model produces a similar velocity distribution as the observations, with the greatest velocities on the inside of the bend, showing that in this bend, the potential flow effect indeed dominates. Sensitivity tests showed that even with significantly reduced depth, increased friction, or greater cross-channel bed slope (representing the influence of a point bar), the velocity maximum remains near the inside of the bend.

c. Lateral salinity gradients

The second verification question is: Can the lateral salinity differences in the bend be explained by the lateral velocity differences acting on the along estuary salinity gradient? To answer this question, we consider the salt transport equation, in a depth-averaged sense

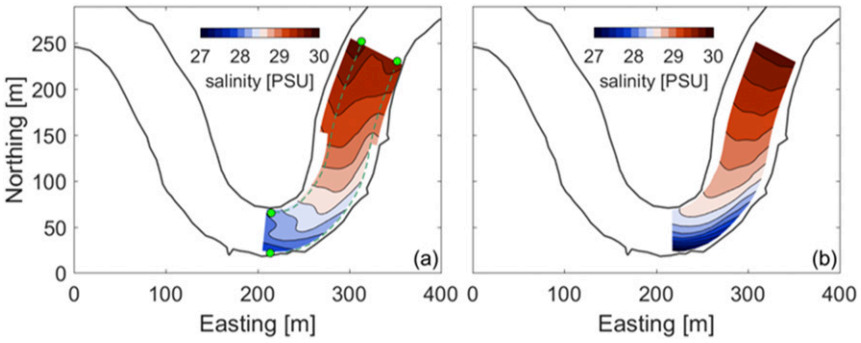

FIG. 11. Salinity (depth averaged): (a) interpolated measurements; (b) calculated from observed streamwise velocities and the cross-sectional averaged salinity at the entrance of the bend as upstream boundary condition. For maximum flood, 25 Jul. Green dots and lines: points of pressure and lines for estimation streamwise momentum.

because of the relatively weak stratification, assuming transport dominated by streamwise advection:

$$\frac{\partial S}{\partial t} = -u\frac{\partial S}{\partial \chi}, \tag{2}$$

(with χ again the along-streamline distance). While the salinity field itself cannot be considered quasi-steady because of the continuous change due to advection by the ebb or flood, on short time scales the salinity is assumed to change everywhere throughout the bend with the same rate, and spatial salinity *differences* are considered quasi-steady ($\partial/\partial t(\partial S/dn) \approx 0$, with n the cross channel coordinate). Using these assumptions, we can relate the lateral salinity gradient anywhere in the bend to the velocity U_0 and along river salinity gradient $\partial S_0/\partial x$ at the entrance of the bend for a given velocity field through

$$\frac{\partial S}{\partial n} = U_0\frac{\partial S_0}{\partial x}\frac{\partial}{\partial n}\int\frac{1}{u}\frac{R+n}{R}ds \tag{3}$$

(with s the along-stream coordinate measured in the centerline and n zero in the centerline; a derivation can be found in appendix B). This expression represents the lateral gradient of the path integral of the along streamline salinity gradient $\partial S/\partial \chi$ from bend entrance to the cross section of interest. Note that not only the lateral velocity shear but also the geometry contributes to generation of the lateral salinity gradient—the increasing pathlength with increasing radius of curvature toward the outside of the bend introduces additional straining of the salinity field.

Here we compare the salinity field upstream (i.e., seaward) of the bend apex as obtained from a linear interpolation of the salinity measurements during flood on 25 July in cross sections 5, 7, and 9 (Fig. 11a), with the salinity distribution that would be generated by the observed velocities if streamwise advection were the only transport mechanism (Fig. 11b). The main result is that streamwise advection of the cross-sectional averaged salinity from the bend entrance leads to a lateral salinity structure that is qualitatively consistent with the observations. Quantitative comparison indicates that near the apex the computed lateral gradient is more than twice that in the interpolated data, indicating that differential advection and the effect of pathlength differences together are more than strong enough to produce the observed lateral salinity gradient. As with the lateral shear, the overestimation of the lateral salinity gradient based on Eq. (3) is consistent with neglecting lateral transport processes that would diminish the lateral gradients. Note that in both the interpolated measurements and in the calculated salinity field the lateral gradients are maximal on the outside of the bend, a result that was found also in the theoretical derivation of $\partial S/\partial n$ (see appendix B) and is a result of the inward skewed velocity distribution as well.

d. Lateral momentum balance

The third question is: Is the observed lateral salinity difference sufficient to generate the observed reversal in secondary circulation? Secondary flow can be computed using the deviation of the depth-dependent lateral momentum from the depth-averaged mean. Due to the quasi-steady flow and strong curvature, temporal acceleration and the influence of Earth's rotation can be neglected. We also neglect frictional effects based on scaling of the frictional forces relative to the centrifugal force ($c_f R/H \approx 3 \times 10^{-2} \ll 1$). This implies that the forcing is not balanced by the internal stress from the vertical profile, but by the nonlinear advective acceleration, which means that the lateral flow is adjusting to the forcing while flowing along the bend (Nidzieko et al. 2009). With these assumptions and leaving out lateral

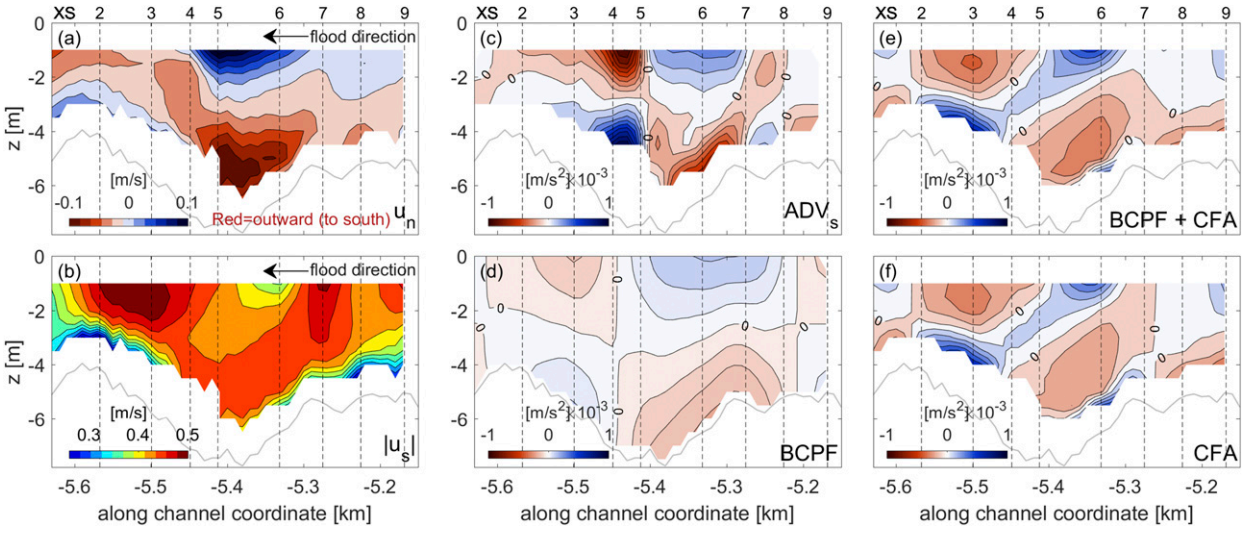

FIG. 12. (a) Lateral velocity u_n, (b) streamwise velocity u_s, (c) advective acceleration (ADV_s), (d) baroclinic pressure gradient force (BCPF), (f) centrifugal acceleration (CFA), and (e) sum of BCPF and CFA, all in the centerline of the river and as function of depth and along-channel coordinate. For maximum flood tide, 25 Jul. Red velocities/accelerations in (a) and (c)–(f) are directed toward the outside of the bend. Contour distances in (c), (e), and (f) are $0.1 \times 10^{-3}\,\mathrm{m\,s^{-2}}$; in (d) it is $0.05 \times 10^{-3}\,\mathrm{m\,s^{-2}}$. Velocities u_s and u_n have been obtained by interpolation of the cross-channel transects, which are numbered above each panel. The BCPF has been calculated using the lateral gradient in the depth-averaged interpolated salinity data, Fig. 11.

and vertical advection, the equation for the secondary circulation becomes

$$\underbrace{\left(u_s\frac{\partial u_n}{\partial s}-\overline{u_s\frac{\partial u_n}{\partial s}}\right)}_{\mathrm{ADV}_s}=\underbrace{\frac{u_s^2-\overline{u_s^2}}{(R+n)}}_{\mathrm{CFA}}-\underbrace{\beta g\left(\int_z^0\frac{\partial S}{\partial n}dz-\overline{\int_{-h}^0\frac{\partial S}{\partial n}dz}\right)}_{\mathrm{BCPF}},\qquad(4)$$

with u_s and u_n the z-dependent streamwise and lateral velocity (bed at $z = -h$), and β the coefficient of saline contraction ($\beta \cong 7.7 \times 10^{-4}$). The left-side term denotes the vertical deviations of the acceleration by streamwise advection (ADV_s), the first right-side term the net (vertically varying) CFA, and the second the BCPF.

To determine how these terms vary through the bend, we consider the along-channel and vertical variations of the quantities of Eq. (4) during a flood tide (Fig. 12). The along-channel distribution of the stream-normal velocity (Fig. 12a) shows again the strong, reversed secondary circulation at the apex (inward at the surface and outward at larger depth), which starts to develop seaward of the apex around cross section 7. Between cross sections 7 and 5 the lateral flow accelerates from 0 to $0.1\,\mathrm{m\,s^{-1}}$ over about 100 m. This along-channel increase in the lateral flow is expressed by the advective acceleration term (Fig. 12c), with acceleration approaching the apex of about $0.4 \times 10^{-3}\,\mathrm{m\,s^{-2}}$. The baroclinic pressure force (Fig. 12d) acts in the same direction as the advective acceleration, that is, it does promote the reversed secondary circulation. However, the salinity-gradient-induced BCPF is only $\sim 0.15 \times 10^{-3}\,\mathrm{m\,s^{-2}}$, which is too small to provide all the momentum for the acceleration.

This discrepancy is explained as follows. Around cross section 6, the streamwise velocity (Fig. 12b) shows a subsurface maximum and reversed vertical shear. This reversed vertical shear causes a reversal in the centrifugal acceleration (Fig. 12d), which starts to exert a force toward the inside of the bend at the surface and toward the outside at larger depth. This promotes the reversed secondary circulation with a magnitude that exceeds the BCPF and is sufficient to give the reversed circulation the observed strength: $ADV_s \approx$ BCPF + CFA (Fig. 12e). [To compare quantitatively: the integrated inward acceleration of the upper water column from BCPF + CFA between cross section 7 and 5 (i.e., the blue area) yields 96% of the integrated inward ADV_s of $5.1 \times 10^{-2}\,\mathrm{m^3\,s^{-2}}$, comparable numbers for the outward acceleration.] We therefore conclude that the reversal in the shear of the streamwise velocity and consequently the CFA is an essential element in generating the reversed secondary flow during flood.

Note that the CFA—unlike the BCPF—will always be inward-directed at the bed where the streamwise

velocity approaches zero. This could explain the near-bed inward-directed velocities found during the neap tide flood survey (Fig. 6d).

e. *The mechanism (part II)—Reversing the vertical shear*

Considering the important role of the reversed shear, a crucial question is–what causes the reversal in shear of the streamwise velocity? Our explanation is as follows: during flood, the baroclinic pressure force first generates a small reversed circulation cell near the outer bank (see Fig. 9, right column). This leads to an inward transport of the lower (streamwise) momentum fluid at the surface and an outward transport of higher-momentum fluid at larger depth. As a result, slow-moving water ends up on top of faster moving water (see Fig. 9, left column), reversing the shear and inducing a centrifugal acceleration that amplifies and expands the reversed circulation cell initially generated by the BCPF. Where the reversed circulation cell meets the ''normal'' circulation cell a surface convergence (observed visually during the measurements as a surface front) leads to downward and subsequently outward transport of higher-momentum fluid, further enhancing the reversed shear. Additionally, the lateral motions generate a small local stratification, which sustains the shear by suppressing vertical mixing. In summary, the BCPF acts like a trigger, activating a reversed CFA that provides the main forcing for the reversed lateral circulation cell.

Why does the reversal of the secondary flow start in the outer part of the cross section? First, the normal centrifugal acceleration is smallest there due to the greater radius of curvature and lower streamwise velocity, while the lateral salinity gradient is greatest there (cf. Fig. 11). This means that the advective acceleration will start to generate reversed circulation at the outside. Next, the slower streamwise flow on the outside of the bend gives the BCPF more time to accelerate the reversed circulation, and provides a reservoir of low-momentum fluid that overrides the high-momentum fluid once the reversed circulation is initiated, which produces the reversal of the vertical shear. During flood this creates a positive feedback: reversed circulation, reversed shear, and enhanced reversed circulation. Note that during ebb the classic secondary circulation, already strengthened by the BCPF, strengthens the shear by advecting faster-moving water from the inside of the bend outward over slow-moving water (e.g., Fig. 8, left column), which enhances the classical circulation. This asymmetry in the interaction with the streamwise shear only enhances the ebb–flood difference in secondary flow.

5. Discussion

a. *Key parameters and comparison with other estuaries*

An essential element for the generation of reversed secondary circulation is the along estuary salinity gradient ($\partial S_0/\partial x$), which is transformed into the lateral salinity gradient by the lateral shear and pathlength difference. The stronger the along-estuary gradient, the stronger the mechanism. This is consistent with the strongest reversed circulation occurring during the neap tide flood, and also explains why classical secondary circulation was observed near the end of the flood during spring tides: the stronger spring flood brought uniformly high-salinity (bay) water into the bend, corresponding with a vanishing along-channel salinity gradient and thus a shutdown of the forcing of the reversed circulation. Also essential is the lateral shear in the streamwise velocity. It mainly results from the competition between the momentum redistribution influences of the free vortex effect and frictional and topographic effects, which is controlled by the frictional parameter $c_f^{-1}H/R$, the relative curvature W/R, and the streamwise curvature variation (Blanckaert and de Vriend 2010; Ottevanger et al. 2012). Channel depth contributes through decreasing frictional and topographical influence on the lateral shear, and also by increasing the baroclinic forcing for a given lateral salinity gradient. Therefore, the reversed circulation is more easily established with increased depth. Curvature ($1/R$) generates the superelevation which induces the lateral shear, but increased curvature also yields increased centrifugal accelerations to overcome, so the strength of the mechanism may not necessarily increase with relative curvature.

To relate our results to other observations, we consider how the North River bend compares with other estuarine bends in parameter space (Table 1), focusing on the relative curvature W/R, the frictional parameter (or relative depth) $c_f^{-1}H/R$, and the ratio of the along-channel and vertical salinity gradients $(\partial S/\partial x)/(\partial S/\partial z)$, scaled with the aspect ratio W/H. The shear ratio $(\partial u/\partial n)/(\partial u/\partial z)$ would also be a valuable quantity for comparison, but it could not be obtained for the other estuarine bends based on the published data. The table shows that the relative curvature W/R and particularly the relative depth $c_f^{-1}H/R$ in the North River bend are significantly greater than in the other cases from the literature, with Elkhorn Slough (Nidzieko et al. 2009) having the next highest values. The aspect ratio W/H is the smallest in the North River and the greatest for Pein et al. (2018). The salinity gradient ratio for the North River is about the same as for Pein et al. (2018), but greater than other cases.

The mechanism observed in the North River is distinctly different from the dynamics in the cases with a

TABLE 1. Overview of parameters and main characteristics for a number of studies on flow in curved estuaries ($c_f = 3 \times 10^{-3}$ has been adopted for all cases). The bold number highlights a result from this study.

Study	Estuary	W/R	$c_f^{-1}H/R$	W/H	$\frac{dS/dx}{\Delta S/\Delta z} \times \frac{W}{H}$	Findings
Chant and Wilson (1997)	Hudson	0.30	1.8	56	0.02	Cross-stream seiche; tilting of pycnocline
Nidzieko et al. (2009)	Elkhorn Slough	0.32	6.0	18	0.04	Three-layer structure; downstream adjustment
Lacy and Monismith (2001)	Snag Channel, SF Bay	0.20	5.3	13	0.12	Reversed circulation in first part ebb; differential advection and junctions
Pein et al. (2018)	Idealized model	0.20	0.7	100	1.00	Reversed circulation at end of flood; BCPF due to differential advection
This study	North River	0.64	**23.8**	9	0.90	Reversed circulation during flood; BCPF due to differential advection

low salinity gradient ratio (Chant and Wilson 1997; Nidzieko et al. 2009). In those cases, stratification is significant and the lateral baroclinic pressure gradient is the result of tilting of the pycnocline by the secondary flow. In the North River, the baroclinic pressure gradient results from the differential streamwise advection, which leads to a greater and more fundamental ebb–flood asymmetry as the differential advection only generates a baroclinic pressure gradient opposing the classical secondary circulation during flood. A similarity between the North River and the Elkhorn Slough is the large role of the advective acceleration (i.e., downstream adjustment), which is related to the large relative depth $c_f^{-1}H/R$ (i.e., limited friction). Snag Channel (Lacy and Monismith 2001) also shows some stratification influence, but that case is predominantly governed by differential advection arising from the confluence of two streams. Like in the North River, laterally sheared streamwise velocities generating ebb–flood asymmetries in the lateral salinity gradient and secondary flow were found also in the numerical study by Pein et al. (2018). However, the meander geometry (W/R, $c_f^{-1}H/R$, W/H) was very different, with significantly lower relative curvature and relative depth. Here, the lateral shear might be explained by the symmetrical cross-sectional depth profile in the idealized estuary, which, like the North River, does not show an inner bend point bar, and in addition has a reduced depth on the outside compared to a more typical outward-skewed depth profile, both promoting an inward-skewed velocity profile.

In summary, the North River bend stands out as a case with extremely high relative depth $c_f^{-1}H/R$ and strong relative curvature W/R, which lead to strong lateral shear. Together with a moderate along-estuary salinity gradient and negligible stratification (at least in the dry season), these conditions provide the necessary elements for the mechanism reversing the secondary circulation during flood tide.

Finally, can we predict the occurrence and strength of the reversed secondary circulation? The reversal is initiated by the lateral baroclinic pressure force overcoming the classical centrifugal acceleration at the outside of the bend, which can be described by the parameter combination

$$\frac{\mathrm{BCPF}}{\mathrm{CFA}} = \gamma \frac{\beta g \dfrac{\partial S_0}{\partial x} H}{U_0^2/R}. \tag{5}$$

Here γ is a parameter that should indicate how efficiently the along-estuary salinity gradient is transformed into a lateral gradient, how the BCPF and CFA near the outside of the bend are related to the values at the centerline, and how the vertical variation of the CFA is related to the depth-averaged force. The first two issues are determined by the lateral shear, the third by the vertical shear. With the lateral shear depending on $c_f^{-1}H/R$, W/R, and the streamwise curvature variation, and assuming that the vertical shear in absence of stratification mainly depends on friction, γ will be a bend-specific parameter, depending on local geometry and friction. It varies between zero for bends where high velocities on the outside of the bend compensate the effect of pathlength differences and no lateral salinity gradient is generated, and order one for bends with an inward skewed velocity distribution dominated by a strong free vortex effect. For our data, we indeed find a strong relationship between the secondary circulation and the parameter combination $\beta g(\partial S_0/\partial x)HR/U_0^2$, which supports using Eq. (5) as indicator of the strength of the reversed circulation. However, it is hard to determine γ values in a prognostic way. Next, Eq. (5) does not account for situations where stratification effects dominate. So Eq. (5) identifies important dependencies but does not yet provide a definite predictive parameter.

b. *Interactions of the secondary flow and morphology*

The large relative depth of the North River can be explained from the high bank stability of the cohesive

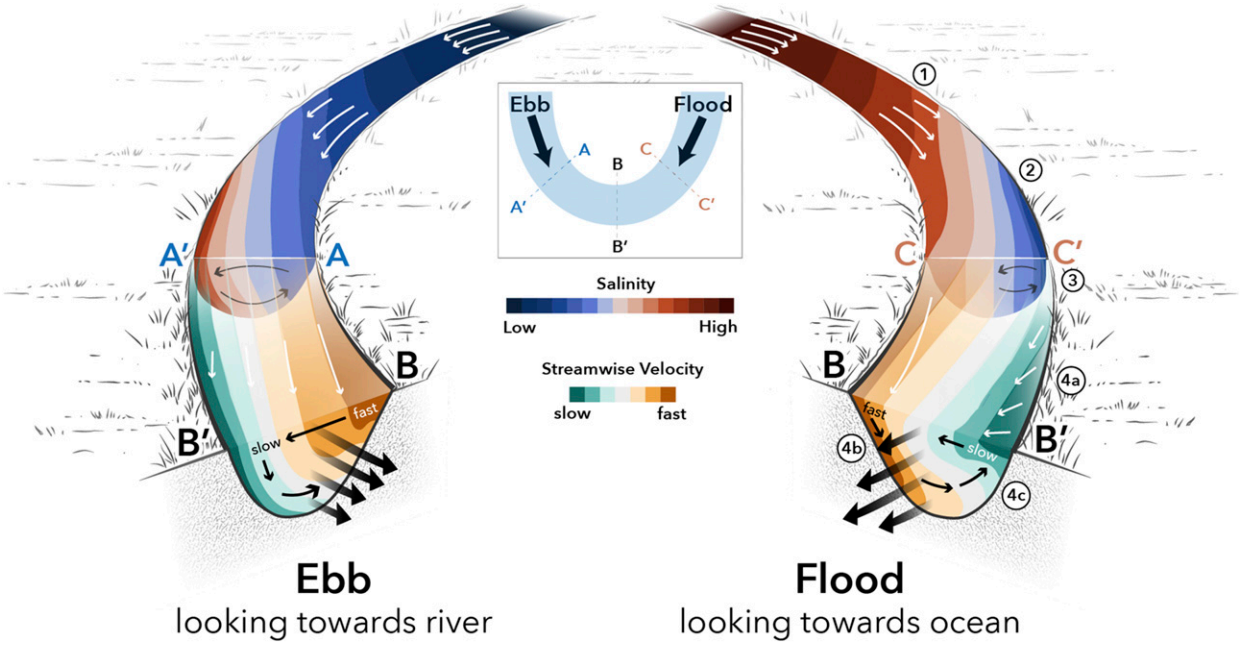

FIG. 13. Schematic of flow and salinity in a sharp estuarine bend under well-mixed conditions. The reversed secondary flow during flood compared to ebb is generated along the following steps: 1) laterally sheared streamwise flow with the greatest velocities near the inside of the bend; 2) lateral salinity differences with the saltiest water near the inside, and the maximum salinity gradient at the outside; 3) a reversal of the secondary circulation in the outer part of the cross section; 4a) transport of water with low streamwise momentum from the outside inward along the surface; 4b) streamwise flow with a subsurface maximum and reversed vertical shear; and 4c) a further increase of the strength and width of the reversed secondary circulation cell.

and vegetated salt marsh (Garofalo 1980). The absence of a distinct point bar in the bend apex might be related to the relatively fine grained sediment of the North River and sharpness and shortness of the bend, resulting in the development, if any, of a point bar downstream of a bend instead of at the apex. In fact, shoals do occur in association with the meanders in the North River, but they are observed only on the seaward side of inner bends, and not on the landward side (see Fig. 1c). This asymmetry may be explained by the ebb dominance of the flow, but it also might be the result of the flow mechanism described in this study: a reversed secondary circulation during flood prevents sediment from being transported along the bed to the inside of the bend to feed the development of the inner bend point bar. The absence of a point bar then allows for the high flow velocities in the inside of the bend, which is an essential condition for the reversed secondary circulation.

6. Conclusions

Our investigation of secondary flow in a salt-marsh estuary with strong curvature indicates some important differences from previous studies of secondary flows in rivers and estuaries, with these significant findings:

1) a distinct difference in the secondary flow between ebb and flood, with circulation as in river bends during ebb, and multiple circulation cells and reversed circulation over a large part of the cross section during flood;
2) streamwise velocity maxima near the inside of the bend during both ebb and flood, and an inward-skewed velocity distribution that is distinctly different from what is generally found in river bends;
3) a salinity anomaly with saltier water in the inside of the bend during flood and fresher water during ebb; and
4) absence of a distinct point bar in the inside of the bend.

The ebb–flood asymmetry in the secondary flow is explained as follows (see Fig. 13): the flow curvature induced water level setup on the outside of the bend and setdown on the inside induces an inward redistribution of the streamwise momentum with decelerating flow toward the apex on the outside and accelerating flow on the inside (potential flow effect). This velocity

structure contrasts with typical river bends, where outward momentum redistribution by frictional and topographic effects overcomes the potential flow effect. Here, that is not the case due to lack of a distinct point bar, and a relatively large cross-sectional depth. The greater streamwise velocity in the inner bend advects water toward the inside of the bend that is fresher than the cross-sectional average during ebb and saltier during flood. This differential advection effect is further enhanced by the pathlength difference between the inside and outside of the bend. The resulting lateral salinity gradient yields a baroclinic pressure gradient force that enhances the classic secondary circulation during ebb and opposes it during flood, arresting and subsequently reversing the secondary circulation when it overcomes the centrifugal forcing. The generation of the reversed circulation during flood first happens in the outer part of the cross section, where the centrifugal force is the smallest and the baroclinic gradient the largest, bringing slower moving water from the outside of the bend inward along the surface. This induces a subsurface maximum and reversed shear in the streamwise velocity and leads to a reversal of the centrifugal force, which subsequently further enhances and expands the reversed secondary circulation cell during flood.

Acknowledgments. This project was funded by NSF Grant OCE-1634490. During this work W.M. Kranenburg was supported as USGS Postdoctoral Scholar at Woods Hole Oceanographic Institution. A.M.P. Garcia was supported by the Michael J. Kowalski Fellowship in Ocean Science and Engineering (AMPG), and the Diversity Fellowship of the MIT Office of the Dean of Graduate Education (AMPG). The authors thank Jay Sisson for the technical support and Peter Traykovski for providing the bathymetric data. Also, the suggestions for improvement by Dr. K. Blanckaert and an anonymous reviewer are thankfully acknowledged.

APPENDIX A

Lateral Distribution of Streamwise Velocity

The model of Blanckaert and de Vriend (2003, 2010) predicts a first-order approximation of the lateral distribution of depth-averaged streamwise velocity based on input for the cross-sectional averaged depth H, cross-sectional width W, radius of curvature R, and parameterized transverse bed level slope A, all as a function of the along channel coordinate. The linear approximation is based on a parameterization of lateral velocity distributions with one degree of freedom:

$$U_s \approx U\left(1+\frac{n}{R}\right)^{\alpha_s} \approx U\left(1+\frac{\alpha_s}{R}n\right), \tag{A1}$$

with U the velocity in the center and α_s a dimensionless number. The model solves α_s/R along the bend from a nonlinear relaxation equation:

$$\lambda_{\alpha_s/R}\frac{\partial}{\partial s}\left(\frac{\alpha_s}{R}\right)+\frac{\alpha_s}{R}=F_{\alpha_s/R}, \tag{A2}$$

with $\lambda_{\alpha_s/R}$ a flow adaptation length (mainly dependent on friction) and $F_{\alpha_s/R}$ the forcing consisting of terms accounting for the momentum redistributing influence of frictional and topographic effects, of streamwise changes in channel curvature (the potential flow effect), and of secondary flow (the latter through a submodel). Note that (for positive R) $\alpha_s = -1$ and $\alpha_s = 1$ respectively correspond to (inward skewed) free vortex and (outward skewed) solid body rotation velocity distributions. See Ottevanger et al. (2012) for a description of the model and earlier applications. The model itself is available at https://svn.oss.deltares.nl/repos/openearthtools/trunk/matlab/applications/meander.

To simulate the studied bend, we used the parameters H, W, and R from Fig. 3, and determined A from the bathymetric data by fitting a linear function through the lateral depth profiles at cross section 1 to 9, (hereby neglecting the outer 5 m on both sides of the profile). With H, W, R, A along the bend and a cross-sectional averaged velocity U in the bend entrance as input, the lateral distribution parameter α_s was computed using the model. To compare this with the data, we also determined α_s from the measured depth-averaged streamwise velocity profiles. This was done in the same way as the determination of A.

A comparison of the measured depth average streamwise velocity, the linear approximation of the data, and the computed velocity profiles is shown in Fig. A1, for the ebb flow of 24 July (i.e., shallow, so largest possible role for friction). Figure A2 shows the data-based and model-computed lateral shear ($U\alpha_s/R$), together with results of runs with adjusted model parameters to explore the sensitivity. The figures show that for both data and model the greatest velocities are found on the inside of the bend. Apparently, the geometry of the bend is in a part of the parameter space where the potential flow effect dominates over the frictional and topographic effects. The sensitivity tests show that even with strongly reduced depth, increased friction, or adapted lateral depth variation (as parameterized by slope A), the velocity maximum remains on the inside of the bend. A reduction in curvature (increased radius) is the factor that most significantly influences the lateral shear.

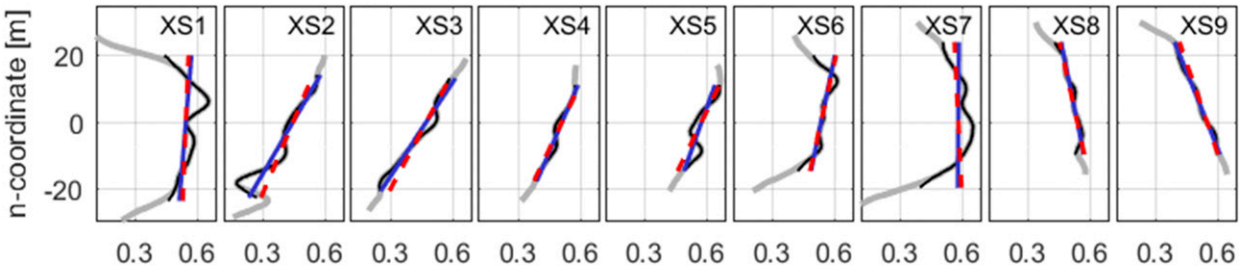

FIG. A1. Streamwise velocity (depth averaged; m s^{-1}; as function of lateral coordinate) for cross sections 1–9, ebb case (24 July). Gray line is data, black line is data neglecting the outer 5 m, blue line is linear approximation of the black line, and red dashed line is model result. The top side (positive n coordinate) is the inside of the bend.

APPENDIX B

Lateral Salinity Gradients in a Curvilinear Coordinate System

a. General case

An expression for the lateral salinity gradient $\partial S/\partial n$ can be formally derived as follows. Assuming advection dominance, the depth-averaged salinity transport equation along any streamline reads

$$\frac{\partial S}{\partial t} = -u\frac{\partial S}{\partial \chi}, \tag{B1}$$

with $\partial\chi$ the along streamline distance, which is related to the along centerline distance through

$$d\chi = \frac{R+n}{R}ds \tag{B2}$$

(so $\partial\chi$ is larger than ds in the outer bend and smaller in the inner bend). Taking the lateral derivative of Eq. (B1) (Chant 2010), and assuming quasi-steady salinity *differences*, we obtain

$$\frac{\partial u}{\partial n}\frac{\partial S}{\partial \chi} = -u\frac{\partial}{\partial n}\left(\frac{\partial S}{\partial \chi}\right). \tag{B3}$$

As $\partial\chi$ is a function of n, we have to substitute Eq. (B2) before we can interchange the derivatives. Using the assumption of quasi-steady salinity difference in combination with the transport equation, the salinity gradient along any streamline can be expressed in the velocity U_0 and along river salinity gradient $\partial S_0/\partial x$ at the entrance of the bend via the local streamwise velocity u:

$$\frac{\partial S}{\partial \chi} = \frac{R}{R+n}\frac{\partial S}{\partial s} = \frac{U_0}{u}\frac{\partial S_0}{\partial x}. \tag{B4}$$

Using these substitutions, Eq. (B3) becomes

$$\frac{\partial u}{\partial n}\frac{U_0}{u}\frac{\partial S_0}{\partial x} = -u\frac{\partial}{\partial n}\left(\frac{R}{R+n}\frac{\partial S}{\partial s}\right). \tag{B5}$$

Elaborating the right side yields

$$\frac{\partial u}{\partial n}\frac{U_0}{u}\frac{\partial S_0}{\partial x} = \frac{uR}{(R+n)^2}\frac{\partial S}{\partial s} - \frac{uR}{(R+n)}\frac{\partial}{\partial s}\left(\frac{\partial S}{\partial n}\right). \tag{B6}$$

Applying Eq. (B4) again, now on the first right side term yields

$$\frac{\partial u}{\partial n}\frac{U_0}{u}\frac{\partial S_0}{\partial x} = \frac{1}{(R+n)}U_0\frac{\partial S_0}{\partial x} - \frac{uR}{(R+n)}\frac{\partial}{\partial s}\left(\frac{\partial S}{\partial n}\right), \tag{B7}$$

which results in an expression for the lateral salinity gradient

$$\frac{\partial S}{\partial n} = U_0\frac{\partial S_0}{\partial x}\left(\int -\frac{1}{u^2}\frac{\partial u}{\partial n}\frac{R+n}{R}ds + \int\frac{1}{uR}ds\right), \tag{B8}$$

which can be written as

$$\frac{\partial S}{\partial n} = U_0\frac{\partial S_0}{\partial x}\frac{\partial}{\partial n}\int\frac{1}{u}\frac{R+n}{R}ds. \tag{B9}$$

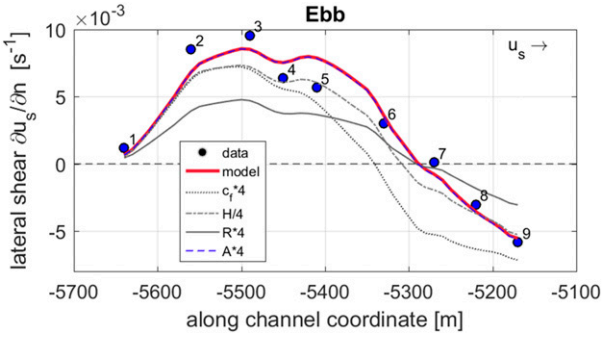

FIG. A2. Lateral shear in the streamwise velocity. Dots are data, the red solid line is the model result, and other lines are results for sensitivity tests with adapted friction c_f, depth H, curvature R, and lateral slope A.

Note that Eq. (B9) is a general expression and that so far no specific velocity field or development of curvature R along the bend has been assumed. The integral basically denotes the travel time from the entrance of the bend, which is the delay time with which the salinity at the entrance arrives at the position (s, n).

b. Special case

Approximating the velocity distribution with a profile function (cf. appendix A),

$$u \approx u_{\mathrm{mid}} \left(\frac{R+n}{R} \right)^{\alpha_s}, \tag{B10}$$

with u_{mid} the streamwise velocity on the centerline (which for α_s is negative can be shown to be slightly smaller than U_0 but assumed equal to U_0 hereafter) and R and α_s still an unknown function of s, and substituting this into Eq. (B9), the lateral salinity gradient becomes

$$\frac{\partial S}{\partial n} = \frac{\partial S_0}{\partial x} \frac{\partial}{\partial n} \int \left(\frac{R+n}{R} \right)^{1-\alpha_s} ds. \tag{B11}$$

For a radius of curvature R and velocity distribution constant throughout the bend, this reduces to

$$\frac{\partial S}{\partial n} = (1-\alpha_s) \frac{\partial S_0}{\partial x} \left(\frac{R+n}{R} \right)^{-\alpha_s} \vartheta, \tag{B12}$$

and for potential flow ($\alpha_s = -1$) to

$$\frac{\partial S}{\partial n} = 2 \frac{\partial S_0}{\partial x} \frac{R+n}{R} \vartheta, \tag{B13}$$

with ϑ the (polar) angle of the cross section of interest in reference to the bend entrance. This expression shows that the velocity itself vanishes from the expression, that the lateral gradient is mainly determined by the along estuary salinity gradient, increases linearly with distance along the bend, and is largest in the outer bend. A measure for the baroclinic pressure gradient is obtained by multiplication with $1/2\beta g H$.

REFERENCES

Apmann, R. P., 1964: A case history in theory and experiment: Fluid flow in bends. *ISIS*, **55**, 427–434, https://doi.org/10.1086/349899.

Blanckaert, K., 2009: Saturation of curvature-induced secondary flow, energy losses, and turbulence in sharp open-channel bends: Laboratory experiments, analysis, and modeling. *J. Geophys. Res.*, **114**, F03015, https://doi.org/10.1029/2008JF001137.

——, 2010: Topographic steering, flow recirculation, velocity redistribution, and bed topography in sharp meander bends. *Water Resour. Res.*, **46**, W09506, https://doi.org/10.1029/2009WR008303.

——, 2011: Hydrodynamic processes in sharp meander bends and their morphological implications. *J. Geophys. Res.*, **116**, F01003, https://doi.org/10.1029/2010JF001806.

——, and H. J. de Vriend, 2003: Nonlinear modeling of mean flow redistribution in curved open channels. *Water Resour. Res.*, **39**, 1375, https://doi.org/10.1029/2003WR002068.

——, and ——, 2004: Secondary flow in sharp open-channel bends. *J. Fluid Mech.*, **498**, 353–380, https://doi.org/10.1017/S0022112003006979.

——, and W. H. Graf, 2004: Momentum transport in sharp open-channel bends. *J. Hydraul. Eng.*, **130**, 186–198, https://doi.org/10.1061/(ASCE)0733-9429(2004)130:3(186).

——, and H. J. de Vriend, 2010: Meander dynamics: A nonlinear model without curvature restrictions for flow in open-channel bends. *J. Geophys. Res.*, **115**, F04011, https://doi.org/10.1029/2009JF001301.

Boussinesq, J., 1868: Mémoire sur l'influence de frottement dans les mouvements réguliers des fluides; xii—essai sur le mouvement permanent d'un liquide dans un canal horizontal axe circulaire. *J. Math. Pures Appl.*, **13**, 377–424.

Buijsman, M. C., and H. Ridderinkhof, 2008: Variability of secondary currents in a weakly stratified tidal inlet with low curvature. *Cont. Shelf Res.*, **28**, 1711–1723, https://doi.org/10.1016/j.csr.2008.04.001.

Chant, R. J., 2002: Secondary circulation in a region of flow curvature: Relationship with tidal forcing and river discharge. *J. Geophys. Res.*, **107**, 3131, https://doi.org/10.1029/2001JC001082.

——, 2010: Estuarine secondary circulation. *Contemporary Issues in Estuarine Physics*, Cambridge University Press, 100–124.

——, and R. E. Wilson, 1997: Secondary circulation in a highly stratified estuary. *J. Geophys. Res.*, **102**, 23 207–23 215, https://doi.org/10.1029/97JC00685.

Dalrymple, R. W., and K. Choi, 2007: Morphologic and facies trends through the fluvial–marine transition in tide-dominated depositional systems: A schematic framework for environmental and sequence-stratigraphic interpretation. *Earth Sci. Rev.*, **81**, 135–174, https://doi.org/10.1016/j.earscirev.2006.10.002.

de Vriend, H. J., and H. J. Geldof, 1983: Main flow velocity in short river bends. *J. Hydraul. Eng.*, **109**, 991–1011, https://doi.org/10.1061/(ASCE)0733-9429(1983)109:7(991).

Dietrich, W. E., and J. D. Smith, 1983: Influence of the point bar on flow through curved channels. *Water Resour. Res.*, **19**, 1173–1192, https://doi.org/10.1029/WR019i005p01173.

Dronkers, J., 1996: The influence of buoyancy on transverse circulation and on estuarine dynamics. *Buoyancy Effects on Coastal and Estuarine Dynamics*, Coastal and Estuarine Studies, Vol. 53, Amer. Geophys. Union, 341–356, https://doi.org/10.1029/CE053p0341.

Engelund, F., 1974: Flow and bed topography in channel bends. *J. Hydraul. Div.*, **100**, 1631–1648.

Fagherazzi, S., E. J. Gabet, and D. J. Furbish, 2004: The effect of bidirectional flow on tidal channel planforms. *Earth Surf. Processes Landforms*, **29**, 295–309, https://doi.org/10.1002/esp.1016.

Friedrichs, C. T., and D. G. Aubrey, 1988: Non-linear tidal distortion in shallow well-mixed estuaries: a synthesis. *Estuarine Coast. Shelf Sci.*, **27**, 521–545, https://doi.org/10.1016/0272-7714(88)90082-0.

Garofalo, D., 1980: The influence of wetland vegetation on tidal stream channel migration and morphology. *Estuaries*, **3**, 258, https://doi.org/10.2307/1352081.

Geyer, W. R., 1993: Three-dimensional tidal flow around headlands. *J. Geophys. Res. Oceans*, **98**, 955–966, https://doi.org/10.1029/92JC02270.

Johannesson, H., and G. Parker, 1989: Velocity redistribution in meandering rivers. *J. Hydrol. Eng.*, **115**, 1019–1039, https://doi.org/10.1061/(ASCE)0733-9429(1989)115:8(1019).

Kalkwijk, J. P. T., and R. Booij, 1986: Adaptation of secondary flow in nearly-horizontal flow. *J. Hydraul. Res.*, **24**, 19–37, https://doi.org/10.1080/00221688609499330.

Lacy, J. R., and S. G. Monismith, 2001: Secondary currents in a curved, stratified, estuarine channel. *J. Geophys. Res.*, **106**, 31 283–31 302, https://doi.org/10.1029/2000JC000606.

Leopold, L. B., and M. G. Wolman, 1960: River meanders. *Bull. Geol. Soc. Amer.*, **71**, 769–794, https://doi.org/10.1130/0016-7606(1960)71[769:RM]2.0.CO;2.

Nakayama, K., D. H. Nguyen, T. Shintani, and K. Komai, 2016: Reversal of secondary flows in a sharp channel bend. *Coastal Eng. J.*, **58**, 1–23, https://doi.org/10.1142/S0578563416500029.

Nidzieko, N. J., J. L. Hench, and S. G. Monismith, 2009: Lateral circulation in well-mixed and stratified estuarine flows with curvature. *J. Phys. Oceanogr.*, **39**, 831–851, https://doi.org/10.1175/2008JPO4017.1.

Nunes, R. A., and J. H. Simpson, 1985: Axial convergence in a well-mixed estuary. *Estuarine Coast. Shelf Sci.*, **20**, 637–649, https://doi.org/10.1016/0272-7714(85)90112-X.

Ottevanger, W., K. Blanckaert, and W. S. J. Uijttewaal, 2012: Processes governing the flow redistribution in sharp river bends. *Geomorphology*, **163–164**, 45–55, https://doi.org/10.1016/j.geomorph.2011.04.049.

Pein, J., A. Valle-Levinson, and E. V. Stanev, 2018: Secondary circulation asymmetry in a meandering, partially stratified estuary. *J. Geophys. Res. Oceans*, **123**, 1670–1683, https://doi.org/10.1002/2016JC012623.

Rozovskii, I. L., 1957: *Flow of Water in Bends of Open Channels*. Academy of Sciences of the Ukrainian SSR, 233 pp.

Seim, H. E., and M. C. Gregg, 1997: The importance of aspiration and channel curvature in producing strong vertical mixing over a sill. *J. Geophys. Res.*, **102**, 3451–3472, https://doi.org/10.1029/96JC03415.

Seminara, G., 2006: Meanders. *J. Fluid Mech.*, **554**, 271, https://doi.org/10.1017/S0022112006008925.

Simpson, J. H., J. Brown, J. Matthews, and G. Allen, 1990: Tidal straining, density currents, and stirring in the control of estuarine stratification. *Estuaries*, **13**, 125, https://doi.org/10.2307/1351581.

Thomson, J., 1877: On the origin of windings of rivers in alluvial plains, with remarks on the flow of water round bends in pipes. *Proc. Roy. Soc. London*, **25**, 5–8, https://doi.org/10.1098/rspl.1876.0004.

Williams, G. P., 1986: River meanders and channel size. *J. Hydrol.*, **88**, 147–164, https://doi.org/10.1016/0022-1694(86)90202-7.

Winterwerp, J. C., Z. B. Wang, T. van der Kaaij, K. Verelst, A. Bijlsma, Y. Meersschaut, and M. Sas, 2006: Flow velocity profiles in the Lower Scheldt estuary. *Ocean Dyn.*, **56**, 284–294, https://doi.org/10.1007/s10236-006-0063-4.